SHORT WAVES IN A ROTATING, SHALLOW TANK WITH BATHYMETRY: A MODEL EQUATION IN THE MILD-SLOPE APPROXIMATION

by

James T. Kirby and Changhoon Lee

RESEARCH REPORT NO. CACR-93-08

October, 1993

Sponsored by NOAA, Office of Sea Grant

CENTER FOR APPLIED COASTAL RESEARCH

Ocean Engineering Laboratory
University of Delaware
Newark, Delaware 19716

SHORT WAVES IN A ROTATING, SHALLOW TANK WITH BATHYMETRY: A MODEL EQUATION IN THE MILD-SLOPE APPROXIMATION*

JAMES T. KIRBY† AND CHANGHOON LEE†

Abstract. A depth-integrated, mild-slope equation for dispersive linear wave motion in a domain under the combined effects of depth variation and rotation is derived. The model reproduces the usual finite-depth mild-slope equation in the absence of rotation and also reproduces the usual long wave approximations when the ratio of wavelength to water depth is large, either with or without the additional effect of rotation. The model could serve as the basis for numerical codes that could compute motions ranging from wind wave refraction to tidal oscillations, without restructuring the internal model coefficients. Refraction and parabolic refraction-diffraction approximations are constructed, and a computational example for wave focusing by a shoal with the effect of rotation is included.

Key words. mild-slope equation, rotational flows, parabolic approximation

AMS subject classifications. 76B15, 76C05, 76U05

1. Introduction. The problem of describing short surface waves in a rotating domain has drawn occasional attention in the literature. By short waves, we mean waves that have significant vertical variations in the structure of the wave-induced velocity and pressure fields. In this connection, Gill (1982, §8.2) mentions that, for the case where the axis of rotation coincides with the vertical axis (in the direction opposing gravity), the solution for a Poincaré wave may be simply extended and gives a dispersion relation

$$\omega^2 = g\lambda \tanh \lambda h, \tag{1}$$

where ω is the angular frequency of the wave in rotating coordinates, h is the water depth, and g is the gravitational acceleration. The number λ is the inverse length scale of the vertical variation of the pressure and horizontal velocity fields, which vary like

$$\frac{\cosh \lambda(h+z)}{\cosh \lambda h}. \tag{2}$$

Finally, λ is related to the wavenumber k ($= 2\pi/L$, where L is the wavelength) according to

$$k^2 = \lambda^2 \left(1 - \epsilon^2\right), \tag{3}$$

where

$$\epsilon = \frac{f}{\omega}. \tag{4}$$

* Received by the editors January 9, 1992; accepted for publication (in revised form) September 22, 1992. This work is a result of research sponsored by National Oceanographic and Atmospheric Administration (NOAA) Office of Sea Grant, Department of Commerce, under grant NA/6RG0162-01 (Project No. R/OE-9). The U.S. Government is authorized to produce and distribute reprints for governmental purposes, notwithstanding any copyright notation that may appear hereon.

† Center for Applied Coastal Research, Department of Civil Engineering, University of Delaware, Newark, Delaware 19716, (kirby@kirby.coastal.udel.edu).

The Coriolis parameter f is twice the angular velocity Ω of the rotating domain and thus ϵ is an inverse Rossby number characterizing the ratio of Coriolis forces to inertial forces, with $\epsilon \to 0$ representing the high-frequency (relative to rotation rate) limit. In addition, we may define the Rossby radius of deformation as $a = \sqrt{gh}/f$. Gill proceeds to question whether the formulation has any relevance to oceanic phenomena, since the Rossby radius is so much larger than h that hydrostatic (long wave) approximations are sufficiently accurate. Thus, domains where both short wave dispersion and rotation effects are important do not seem to overlap for flows on the earth's surface.

More recently, Tsay (1991) attempted to develop a model for linear waves, such as short Poincaré waves, in domains having depth variations that are relatively slow in comparison to the wavelength. The desire for such a model grows out of the existence of the mild slope equation of Berkhoff (1972) and Smith and Sprinks (1975) for the case of irrotational flow in a nonrotating domain, which proved to be a highly valuable resource in the development of wave propagation models for intermediate water depths. The existence of such a model would provide the basis for numerical codes that could be applied both to short wave and long rotational wave problems with no alteration of model parameters. However, it is also true that the mild-slope equation should pass identically into the long wave equations in the low-frequency limit. This condition is met in the irrotational case, but the rotational model of Tsay does not pass correctly into the appropriate long wave limit (see Kirby (1992)). Tsay's model is also only appropriate for flows in the neighborhood of the earth's poles, owing to the structure of the fluid acceleration terms, which were incorrect for domains where the vertical coordinate deviates from the axis of rotation.

Since the existence and behavior of short surface waves may still be of some interest and importance in tanks that are rotating relatively rapidly, we correct the deficiencies in Tsay's original formulation in §2, where we arrive at a wave equation as well as a reduced elliptic equation. These equations extend the mild-slope equation to include rotational effects. The correspondence to previously developed models in the long wave limit is also demonstrated. In §3 we consider an eikonal transport and ray approximation for waves in a slowly varying domain and examine the refraction of plane Poincaré waves over a planar topography. To study diffraction effects in the neighborhood of caustics of the geometric optics formulation, we specify a lowest-order parabolic approximation for the combined refraction-diffraction of forward scattered waves in §4. We demonstrate that Kelvin waves may be exactly described by the lowest-order parabolic approximation being used and study the scattering of plane Poincaré waves by a circular shoal. Finally, we consider the scattering of a plane Poincaré wave by an impermeable vertical boundary and compare parabolic model computations to analytic results given by Chambers (1964).

2. Theoretical formulation. We consider the motion of an inviscid, incompressible fluid with a free surface in a rotating domain. The axis of rotation z coincides with the vertical axis pointing opposite to the direction of gravity. The horizontal coordinates (x, y) lie in the plane of the free surface, as indicated in Fig. 1. We consider centripetal effects to be small enough to neglect. We first develop particularly useful forms of the governing equations and then use these forms to derive a depth-integrated model equation.

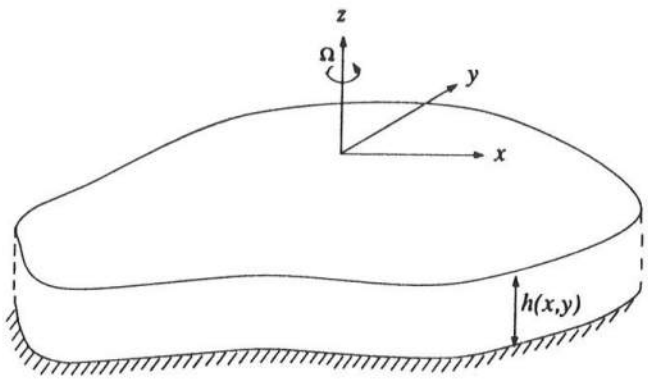

FIG. 1. *Definition sketch.*

2.1. Governing equations. The governing equations for the linearized perturbations to the hydrostatic rest state are given by

$$u_t - fv + \frac{1}{\rho}p_x = 0, \tag{5}$$

$$v_t + fu + \frac{1}{\rho}p_y = 0, \tag{6}$$

$$w_t + \frac{1}{\rho}p_z = 0, \qquad -h(x,y) \le z \le 0, \tag{7}$$

together with

$$u_x + v_y + w_z = 0. \tag{8}$$

Subscripts x, y, z, and t denote partial derivatives. Taking the divergence of the momentum equation gives

$$\nabla^2 p = \rho f(v_x - u_y), \tag{9}$$

where $\nabla^2(\cdot) = \{(\cdot)_{xx} + (\cdot)_{yy} + (\cdot)_{zz}\}$ is the Laplace operator. Differentiating (9) twice with respect to time and using (5)–(8) gives a governing equation for p alone,

$$\nabla^2 p_{tt} + f^2 p_{zz} = 0, \qquad -h(x,y) \le z \le 0, \tag{10}$$

which we adopt as the basic governing equation. Equation (10) gives Laplace's equation for the pressure field in the absence of rotation.

The kinematic condition at the bottom boundary is given by

$$w = -h_x u - h_y v, \qquad z = -h(x,y). \tag{11}$$

Again, by differentiating (11) three times with respect to time and using the momentum equations, we obtain

$$(p_z + \nabla_h h \cdot \nabla_h p)_{tt} + f^2 p_z + f J(h,p)_t = 0, \qquad z = -h(x,y), \tag{12}$$

where ∇_h denotes a gradient in horizontal coordinates and where

$$J(h,p) = h_x p_y - h_y p_x = |\nabla_h h \times \nabla_h p| \tag{13}$$

is the Jacobian of h and p. The linearized kinematic surface boundary condition is

$$\eta_t = w, \qquad z = 0. \tag{14}$$

where η is the local free surface displacement. The linearized dynamic condition reduces to

$$p = \rho g \eta, \qquad z = 0. \tag{15}$$

Combining (14), (15), and (7) gives

$$p_{tt} + g p_z = 0, \qquad z = 0. \tag{16}$$

Equations (10), (12), and (16) provide the boundary value problem for the linearized perturbation to the hydrostatic pressure distribution arising from small amplitude surface wave motion.

2.2. The model equation. Following the work of Berkhoff (1972) and Smith and Sprinks (1975), we now reduce the three-dimensional boundary value problem to a model equation for waves of nearly constant frequency in the horizontal plane of the surface. The procedure adopted by Smith and Sprinks consists of identifying the constant-depth solution to (10), (12), and (16) as a local approximation to the variable depth solution. We then multiply (10) by the vertical structure of p and integrate over the depth to obtain a weighted residual approximation, leaving a governing differential equation in (x, y, t). Following the discussion in §1, we take

$$p(x, y, z, t) = \tilde{p}(x, y, t) F(z), \tag{17}$$

where

$$F(z) = \frac{\cosh \lambda(h + z)}{\cosh \lambda h}. \tag{18}$$

The parameter λ is related to the angular frequency ω according to (1), above, while λ is related to the wavenumber k by (3). From (15), we obtain

$$\tilde{p} = \rho g \eta. \tag{19}$$

Then, multiplying (10) by $F(z)$, integrating over the depth and using the surface and bottom boundary conditions gives

$$\eta_{ttt} - \nabla_h \cdot (g F_1 \nabla_h \eta_t) + \epsilon^2 \omega^2 \eta_t + g F_2 \left(1 - \epsilon^2\right) \eta_t - \frac{\epsilon g \omega}{\cosh^2 \lambda h} J(h, \eta) = 0, \tag{20}$$

where terms that are second-order in bottom slope have been neglected, where

$$F_1 = \int_{-h}^{0} F^2 dz = \frac{\tanh \lambda h}{2\lambda} \left(1 + \frac{2\lambda h}{\sinh 2\lambda h}\right), \tag{21}$$

$$F_2 = \int_{-h}^{0} (F_z)^2 dz = \frac{\lambda \tanh \lambda h}{2} \left(1 - \frac{2\lambda h}{\sinh 2\lambda h}\right) = \frac{\omega^2}{g} - \lambda^2 F_1, \tag{22}$$

and where ϵ is defined in (4). Equation (20) is the final time-dependent form of the model equation. The model may be reduced further to an elliptic form using the substitution

$$\eta(x, y, t) = \hat{\eta}(x, y) e^{-i\omega t}. \tag{23}$$

Substituting (23) into (20) gives

$$\nabla_h \cdot (gF_1 \nabla_h \hat{\eta}) + gk^2 F_1 \hat{\eta} + i \frac{g\epsilon}{\cosh^2 \lambda h} J(h, \hat{\eta}) = 0, \tag{24}$$

where k is defined in (3).

We end this section by remarking that that motion described by the boundary value problem (10), (12), (16), or by the model equation (20) is essentially vortical for the case of a rotating domain ($\epsilon \neq 0$). For strictly periodic motions with angular frequency ω, the velocity components are given by

$$u = \frac{gF(z)}{\omega(1-\epsilon^2)} \left(-i\eta_x + \epsilon \eta_y\right), \tag{25}$$

$$v = \frac{gF(z)}{\omega(1-\epsilon^2)} \left(-i\eta_y - \epsilon \eta_x\right), \tag{26}$$

$$w = -i \frac{gF_z(z)}{\omega} \eta. \tag{27}$$

The vorticity is given by

$$\vec{\omega} = \nabla \times \mathbf{u} = \frac{\epsilon g}{\omega(1-\epsilon^2)} \left[F_z(\eta_x + i\epsilon\eta_y), F_z(\eta_y - i\epsilon\eta_x), -F\nabla_h^2 \eta\right]. \tag{28}$$

The vorticity vanishes in the limit $\epsilon \to 0$, recovering the irrotational mild-slope approximation.

2.3. Comparison to previous results. The elliptic form of the model (24) reduces to Berkhoff's equation in the limit $\epsilon \to 0$, as expected. The model equation derived by Tsay (1991) lacks the third term in (24), and so his model cannot be taken to be an appropriate model for rotational waves unless depth is constant or the water is effectively deep (λh large).

It is also revealing to look at the various limits of the time-dependent equation (20). In the long wave limit ($\lambda h \to 0$), we have $F_1 \to h$ and $F_2 \to 0$. The appropriate limiting form of the model is then

$$(\eta_{tt} + \epsilon^2 \omega^2 \eta)_t - \nabla_h \cdot (gh \nabla_h \eta)_t - \epsilon g \omega J(h, \eta) = 0, \tag{29}$$

which is the usual form for the linearized rotating shallow water wave equation (see Pedlosky (1979, p. 69)). In the absence of rotation, (20) may be integrated once in time to obtain the result

$$\eta_{tt} - \nabla_h \cdot (CC_g \nabla_h \eta) + \left(\omega^2 - k^2 CC_g\right) \eta = 0, \tag{30}$$

where C and C_g are the phase and the group velocities for linearized irrotational surface waves. This equation was given originally by Smith and Sprinks (1975).

3. Geometric optics approximations for shoaling and refracting waves. For the case where variation in the wave train is very slow relative to variations in the domain topography, the propagation of short surface waves is often treated from the geometric optics point of view, which leads to the usual ray approximation.

The geometric optics approximation is constructed by substituting the ansatz

$$\hat{\eta} = a(x, y) \mathrm{e}^{i\psi(x,y)}, \tag{31}$$

where a is a real amplitude and ψ a real phase function, in (24). Separating the real and imaginary part of the resulting equation leads to an eikonal equation for the phase function

$$(\nabla_h \psi)^2 = k^2 - \frac{\epsilon}{F_1 \cosh^2 \lambda h} J(h, \psi) + \frac{\nabla_h \cdot (F_1 \nabla_h a)}{F_1 a} \tag{32}$$

and a transport equation for wave energy

$$\nabla_h \cdot (a^2 F_1 \nabla_h \psi) + \frac{\epsilon}{2 \cosh^2 \lambda h} J(h, a^2) = 0. \tag{33}$$

For the case of irrotational short waves, it is usually assumed that, for bottom slopes of small size, the last term in (32) is second order in the small parameter and thus negligibly small (see Keller (1958)). Retention of the term allows for the inclusion of weak diffraction corrections in grid-based refraction schemes. In the present case, we see that the inclusion of rotation leads to an additional term in (32), based on the Jacobian, which remains at first order in the bottom slope and thus is more important than the neglected diffraction effects. Neglecting terms that are second-order small leads to the geometric optics approximation

$$(\nabla_h \psi)^2 = k^2 - \frac{\epsilon}{F_1 \cosh^2 \lambda h} J(h, \psi) \tag{34}$$

and

$$\nabla_h \cdot (a^2 F_1 \nabla_h \psi) = 0. \tag{35}$$

For straight and parallel bottom contours with x direction normal to the slope, we study the spatial evolution of amplitude $a(x)$. The phase function is given by

$$\psi(x, y) = \Psi(x) + my, \tag{36}$$

where m is the longshore wavenumber and is constant. The geometric optics approximation reduces to

$$\Psi_x^2 = k^2 - m^2 - \frac{\epsilon h_x m}{F_1 \cosh^2 \lambda h}, \tag{37}$$

$$\frac{a}{a_0} = \sqrt{\frac{F_{1_0}}{F_1} \frac{\Psi_{x_0}}{\Psi_x}}, \tag{38}$$

where the subscript 0 denotes a reference incident wave condition. For Poincaré waves, F_1 can be rewritten as

$$F_1 = \frac{CC_g}{g}(1 - \epsilon^2), \tag{39}$$

where C and C_g are the local phase and group velocities. Equation (38) becomes

$$\frac{a}{a_0} = \sqrt{\frac{C_{g_0}}{C_g}} \sqrt{\frac{\Psi_{x_0}}{k_0} \frac{k}{\Psi_x}} = K_s K_r, \tag{40}$$

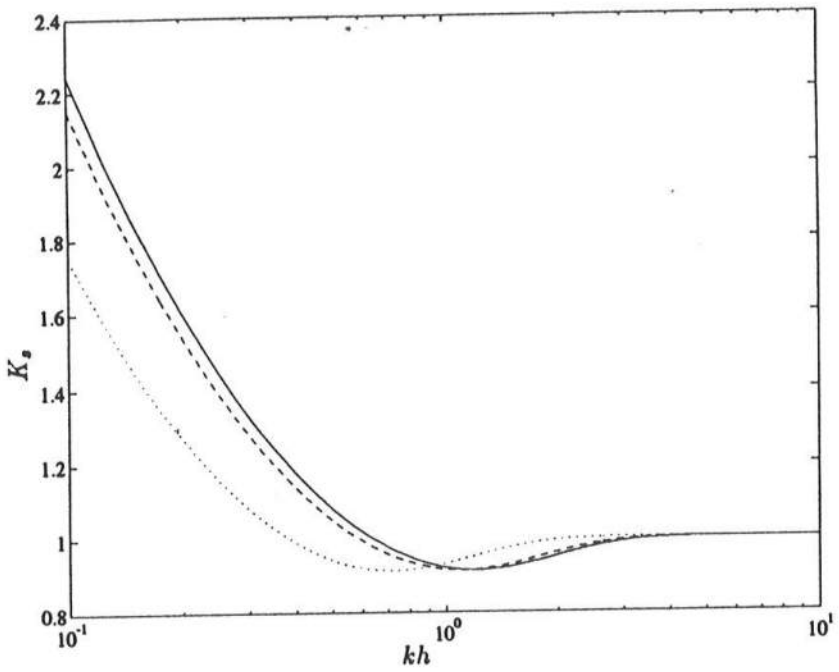

FIG. 2. *Shoaling coefficient for Poincaré waves over a slope.*

where the first and the last terms in the right-hand side are shoaling and refraction coefficients, respectively.

Figure 2 shows a plot of shoaling coefficient K_s as a function of kh for several different rotation rates. Rotation, which shortens the vertical profile of the wave-induced velocity field, causes a shoreward shift of the shoaling curves which becomes pronounced as ϵ approaches unity. Otherwise, the form of the curve is unaltered from the irrotational case.

Refraction coefficients with rotation effects are larger than with no rotation effects in the whole range of kh, approaching unity at large values of kh. An inspection of (37) and (40) shows that the refraction coefficient is dependent on angle of incidence and beach slope as well as the rotation rate. Figures 3(a) and 3(b) show results for K_r and $K_s K_r$ for a case with a mild slope $h_x = 0.1$, in which the importance of the Jacobian term is minor. The refraction coefficient shows a strong dependence on angle of incidence θ_0 and a weaker dependence on rotation rate (except at large ϵ, where the effect is similar to the effect on the shoaling coefficient.) In contrast, Figs. 4(a) and 4(b) show results for a much more severe slope, $h_x = 0.55$. In this case, refraction coefficients take on values larger than unity for a wide range of parameters. A strong peak in the coefficient near $kh = 1$ is noted for $\epsilon = 0.8$. This peak occurs because the value of Ψ_x becomes locally small. For more severe bottom slopes, the value of Ψ_x can take on zero or imaginary values, indicating the formation of a pair of turning points in the governing differential equation. These turning points correspond to caustic lines parallel to the topography in the geometric optics approximation. For these cases, waves incident from offshore would be reflected at the deeper caustic location, while waves originating in shallower water could be totally reflected at the shallower caustic location. This case differs from the case of total reflection of a wave

propagating toward deep water, in that the reflection could occur at a small value of kh in either the intermediate depth or long wave approximations. Figure 5 gives a plot of values of $(\Psi_x/k)^2$ for a range of parameters. The appearance of turning points, associated with zeros of the plotted curves, is apparent for the large bottom slope cases.

In reality, diffraction effects would become strong and would modify the wave height predictions near the caustic positions. We do not consider this effect further here, in favor of moving to the development of a parabolic approximation, which will allow for the treatment of caustics over an arbitrary topography.

4. A parabolic approximation for forward-propagating waves. Wave propagation in a domain with a predominant direction and little backscatter may be modelled using a parabolic approximation of the elliptic boundary value problem (see Radder (1979)). In this section, we establish the standard small-angle parabolic approximation for the elliptic model (24) and apply it to the study of wave focusing and diffraction by a submerged bump. The effect of increasing rotation on the scattering process is examined. We also extend a recent result of Dalrymple and Martin (1992) to provide transmitting lateral boundary conditions for the computational domain. The transmitting boundaries allow complete transmission of the scattered waves arising inside the computational domain.

4.1. The parabolic equation. Considering the dominant direction of wave propagation to be the x direction, let $\hat{\eta}$ be written as

$$\hat{\eta}(x,y) = A(x,y)e^{ik_0 x}, \tag{41}$$

where k_0 is a constant reference wavenumber and A is a complex amplitude. Substituting (41) into (24) gives

$$\begin{aligned}(F_1 A_x)_x + (F_1 A_y)_y + \left\{(k^2 - k_0^2)F_1 + \frac{k_0\epsilon}{\cosh^2 \lambda h} h_y\right\} A \\ + i\left\{k_0 F_{1x} A + 2k_0 F_1 A_x + \frac{\epsilon}{\cosh^2 \lambda h}(h_x A_y - h_y A_x)\right\} = 0.\end{aligned} \tag{42}$$

To construct the parabolic approximation, we assume that the direction of travel of all waves in the computational domain deviates only a small amount from the x direction. Taking $\delta \ll 1$ to characterize the size of the angular deviation away from the x direction, the scales of A_x and A_y are given by

$$\left|\frac{A_x}{k_0 A}\right| \sim O(\delta^2), \qquad \left|\frac{A_y}{k_0 A}\right| \sim O(\delta). \tag{43}$$

We assume that

$$\frac{|\nabla_h h|}{k_0 h} = O(\delta^2), \tag{44}$$

which restricts the depth variations to be slow relative to the surface wavelength. Then, ignoring the terms smaller than $O(\delta^2)$ in (42) leads to

$$\begin{aligned}F_1 A_{yy} + \left\{F_{1y} + i\frac{\epsilon}{\cosh^2 \lambda h} h_x\right\} A_y + 2ik_0 F_1 A_x \\ + \left\{(k^2 - k_0^2)F_1 + \frac{k_0\epsilon}{\cosh^2 \lambda h} h_y + ik_0 F_{1x}\right\} A = 0,\end{aligned} \tag{45}$$

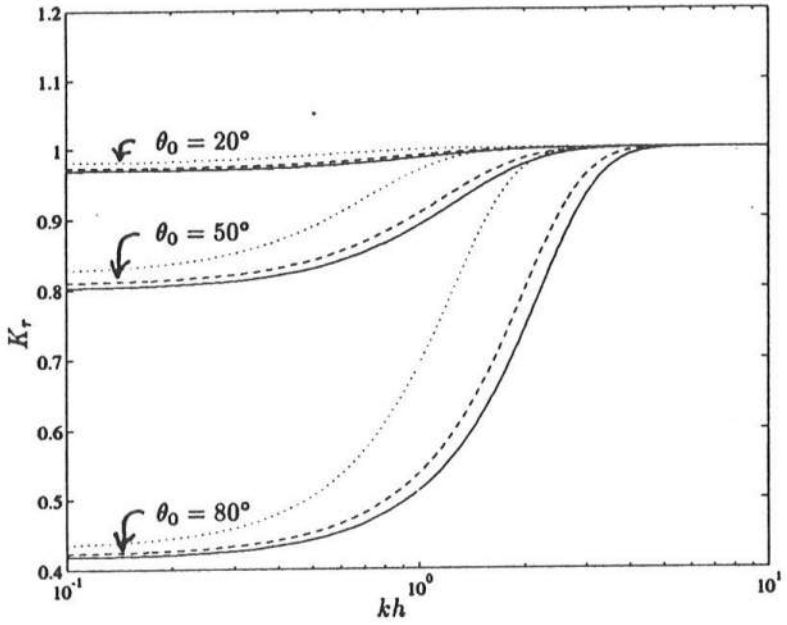

(a)

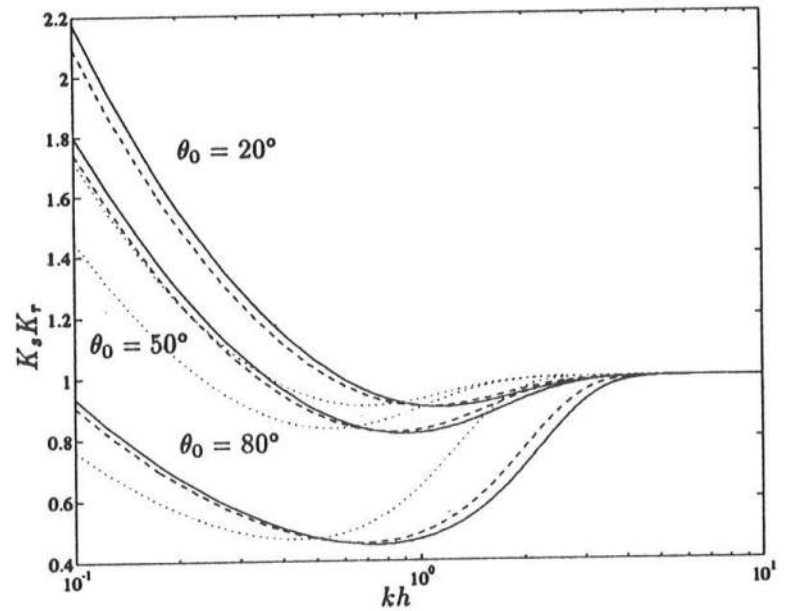

(b)

FIG. 3. *Refraction coefficient and wave height change for waves refracting over a slope:* $h_x = 0.1$, (a) K_r, (b) $K_s K_r$.

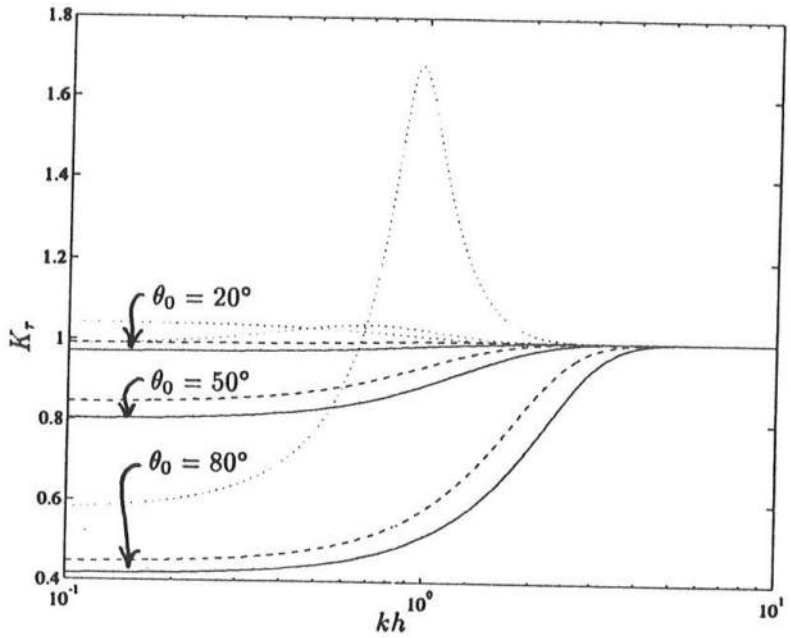

(a)

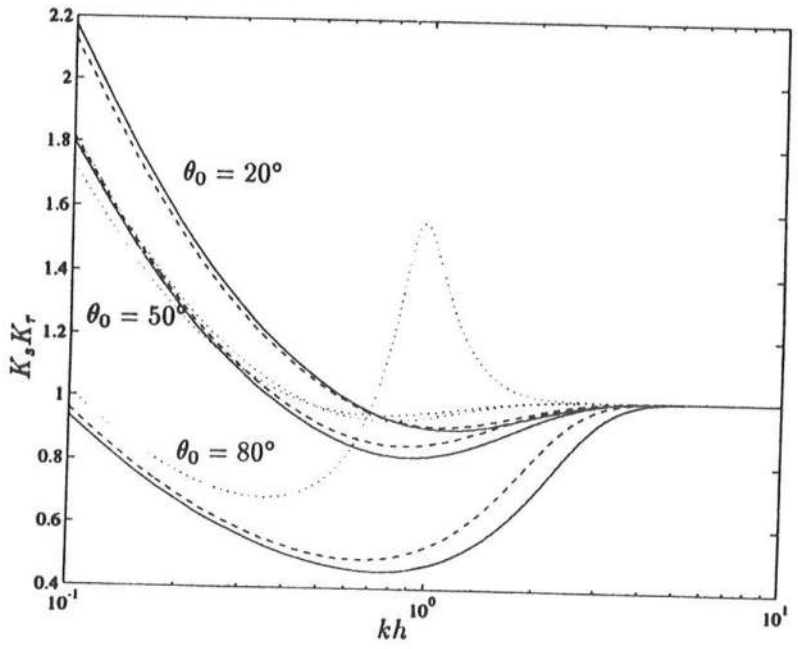

(b)

FIG. 4. *Refraction coefficient and wave height change for waves refracting over a slope:* $h_x = 0.55$, (a) K_r, (b) $K_s K_r$.

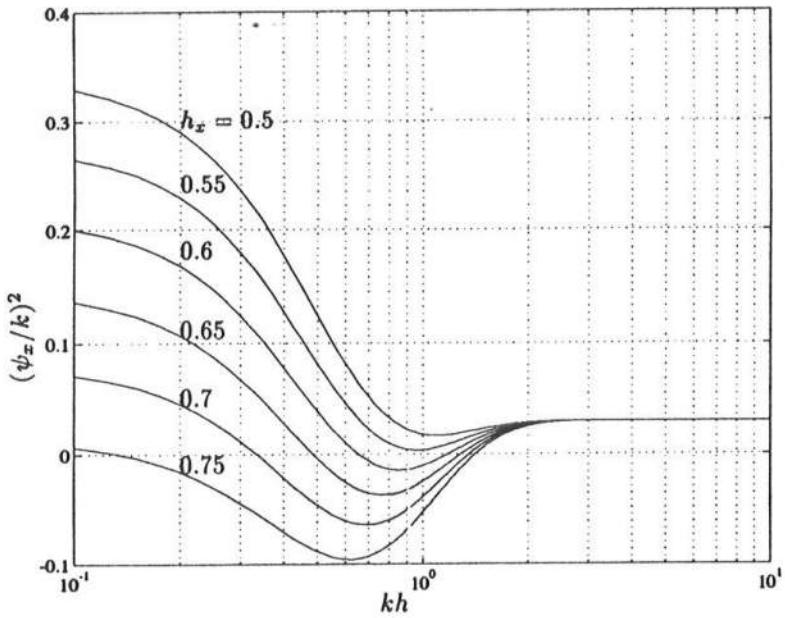

FIG. 5. *x component of wavenumber for refracting and shoaling waves with rotation effects.*

which is the parabolic equation for A. A standard Crank–Nicolson finite difference scheme is used to discretize (45).

4.2. Treatment of lateral boundaries. We use two boundary conditions along the lateral boundaries. One is the closed boundary condition in which there is a perfect reflection along the boundaries. For the case of propagation in a rotating domain with boundaries oriented along the x direction, the lateral boundary condition on $\hat{\eta}$ may be written as

$$\hat{\eta}_y - i\epsilon\hat{\eta}_x = 0. \tag{46}$$

Substituting expression (41) for $\hat{\eta}$ and dropping the smallest term gives the model boundary condition

$$A_y + k_0\epsilon A = 0. \tag{47}$$

The other boundary condition studied here is the open, transmitting boundary condition developed by Dalrymple and Martin (1992), who used this condition for the simple parabolic equation

$$\tilde{A}_{yy} + 2ik_0\tilde{A}_x = 0. \tag{48}$$

The boundary condition may be written as

$$\begin{aligned} &\frac{\partial \tilde{A}(x,y_b)}{\partial y} - \frac{\partial \tilde{A}_{\text{inc}}(x,y_b)}{\partial y} \\ &\qquad = iK\int_0^x \frac{\partial \tilde{A}(\xi,y_b)}{\partial \xi}\frac{d\xi}{\sqrt{x-\xi}} - iK\int_0^x \frac{\partial \tilde{A}_{\text{inc}}(\xi,y_b)}{\partial \xi}\frac{d\xi}{\sqrt{x-\xi}}, \end{aligned} \tag{49}$$

where $\tilde{A}_{\text{inc}}$ is an incident wave amplitude, y_b is the y-coordinate of the boundaries, and $K = \sqrt{2ik/\pi}$. The condition requires the evaluation of an integral along each lateral boundary. For constant water depth along the boundaries, the present model (45) reduces to the form

$$A_{yy} + 2ik_0 A_x + \alpha A = 0 \tag{50}$$

at the boundaries, where

$$\alpha = k^2 - k_0^2 \tag{51}$$

is a constant. The equation for A may be reduced to the simple parabolic equation for $\tilde{A}$ by the transformation

$$A = \tilde{A} e^{i\alpha x/2k_0}. \tag{52}$$

Note that, if k_0 is defined to be the wavenumber for the constant depth region away from the shoal, then α is identically zero, and no transformation is required.

4.3. Representation of Kelvin waves in the parabolic model. In a domain with constant depth and closed lateral boundaries, the parabolic equation is, from (45),

$$2ik_0 A_x + A_{yy} + (k^2 - k_0^2)A = 0 \tag{53}$$

with the boundary condition (47). Let k_0 be given by

$$k_0 = \lambda. \tag{54}$$

Substituting (54) into (53) and (47) gives

$$A = ae^{-\epsilon\lambda y} \tag{55}$$

and

$$\hat{\eta} = ae^{i\lambda x - \epsilon\lambda y}, \tag{56}$$

where a is an arbitrary real amplitude. Equation (56) is the exact solution for a Kelvin wave, which also arises from the full elliptic equation. This result is of some interest, since it represents a case where a parabolized wave equation reproduces an exact solution, even though the wave being represented has transverse variations in its properties. The success of the approximation here is likely due to the fact that the motion associated with the Kelvin wave is purely unidimensional and is oriented in the preferred x direction. The solution is also only correct if the choice (54) is made; any other choice leads to errors in the wavelength and transverse decay rate.

4.4. Scattering of Poincaré wave by a circular shoal. As an example of the numerical application of the parabolic equation to a wave scattering problem, the propagation of an incident plane wave over a circular symmetrical shoal with parabolic bottom slope is considered. The depths in the computational domain are described by

$$h = \begin{cases} h_m + (h_0 - h_m)\dfrac{r^2}{R^2} & \text{for } r \le R, \\ h_0 & \text{for } r \ge R, \end{cases} \tag{57}$$

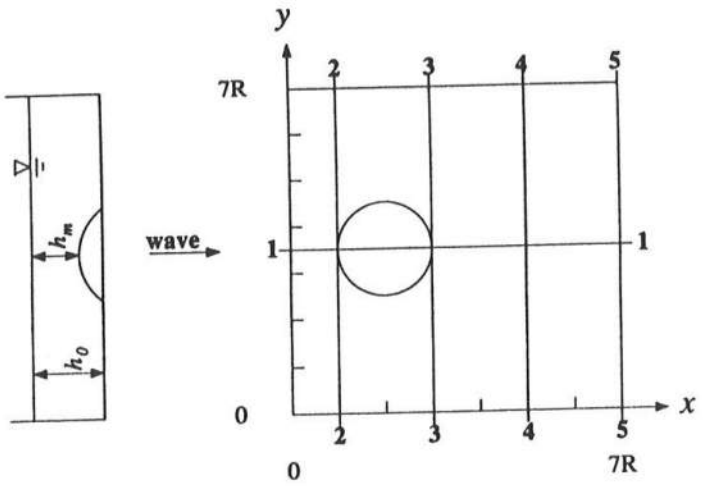

FIG. 6. *Domain for parabolic model computations.*

where

$$r^2 = (x - x_m)^2 + (y - y_m)^2, \tag{58}$$

$$h_m = \tfrac{1}{3} h_0. \tag{59}$$

The geometry of the model domain is illustrated in Fig. 6. We assume that, when there are no rotation effects,

$$\frac{L_0}{R} = 1, \qquad k_0 h_0 = \frac{1}{2}, \tag{60}$$

where L_0 is the initial wavelength, and vary the rotation effect ϵ over the values $\epsilon =$ 0, 0.4, 0.8. The reference value of λ for the incident wave is held fixed, so that k_0 varies with rotation rate. This choice causes the depth of penetration of the wave to remain constant as the rotation rate is varied. As a result, the incident wavelength increases with increasing rotation.

The numerical grid spacing is given as

$$\Delta x = \Delta y, \qquad R = 32 \Delta x. \tag{61}$$

An incident wave enters the domain in the positive x direction. When there is no rotation effect, the initial relative water depth, $k_0 h_0 = 0.5$, means that the depth is intermediate.

Figures 7(a)–(d) show several transects of waveheight normalized by incident values along the indicated lines in Fig. 6. The lateral boundaries are taken to be open in this case. The effect of rotation is to deflect the wave focal pattern to the left of the direction of propagation, causing an increasingly asymmetric wave pattern as rotation increases. The efficiency of the open lateral boundary condition (50) in allowing the scattered waves to exit the computational domain is also apparent. A plan view of the surface profile of the scattered wave field for $\epsilon = 0.8$ is shown in Fig. 8. The asymmetry of the wave pattern is seen to develop strongly over the shoal

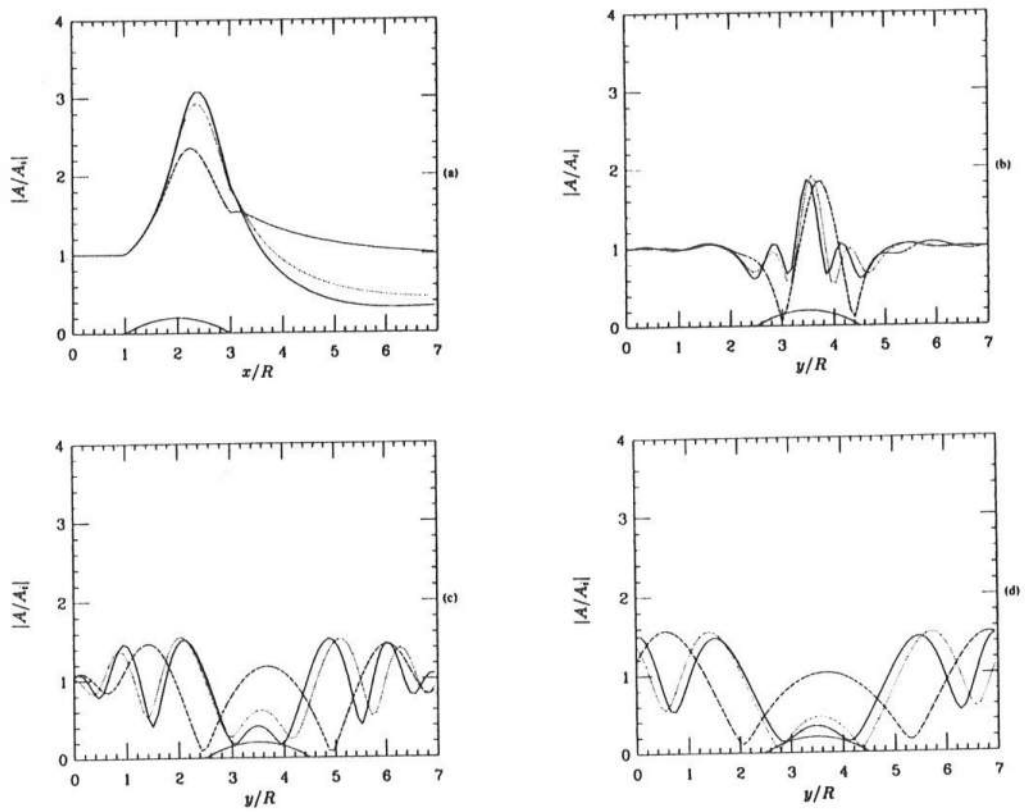

FIG. 7. *Normalized wave heights for waves over a circular shoal; open boundaries.* (a) $y/R = 3.5$. (b) $x/R = 3$, (c) $x/R = 5$, (d) $x/R = 7$.

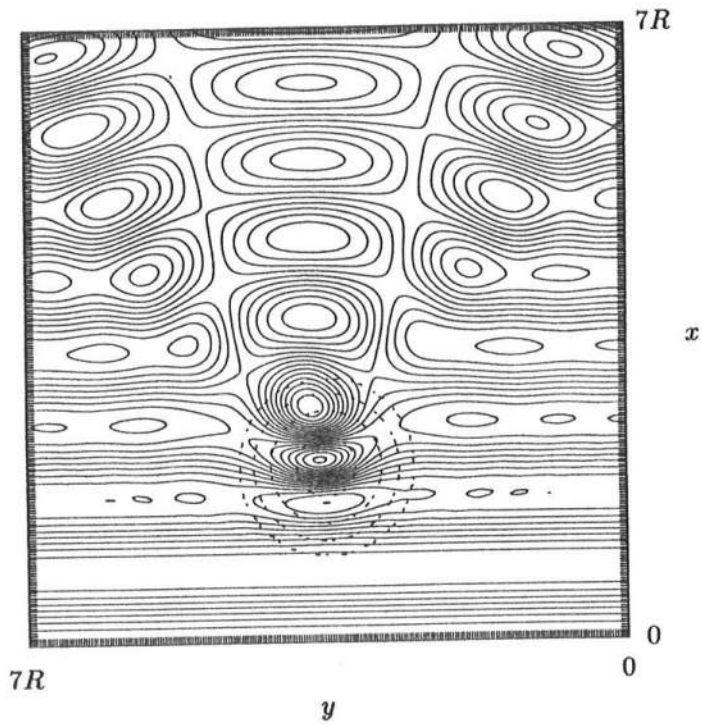

FIG. 8. *Surface elevation contours for wave scattered by a circular shoal; open boundaries,* $\epsilon = 0.8$.

(indicated by dashed contour lines) but regains a more x-directed orientation in the flat region downwave of the shoal.

Figures 9(a)–(c) show three transects across the channel for the case where a plane Poincaré wave propagates into a channel with rigid vertical boundaries. In this case, there is initial diffraction of the wave field at the boundaries and the evolution of a Kelvin wave pattern on the boundary to the right of the direction of propagation. This effect is noticeable immediately in Fig. 9(a), where the transect is upwave of the shoal. On the left boundary, a reduction of the wave height occurs, which would also be consistent with the pattern of a Kelvin wave in the channel. These diffraction patterns persist down the channel and eventually are superimposed on the scattered wave field, which evolves due to interaction with the shoal. Figure 10 shows the instantaneous surface contours for the present case. The development of the Kelvin wave at the right boundary and its subsequent interaction with the scattered wave field is evident. Since the value of k_0 is taken to be k on the boundary (rather than λ), the resulting Kelvin wavelength is not accurately predicted. There is also a certain amount of high wavenumber noise superimposed on the wave field, which is apparent in the figure. This noise develops due to the sharp changes in wave height that occur at the initial interaction of the plane wave with the lateral boundaries. The propagation of spurious high wavenumber components in two parabolic model schemes has been discussed previously by Kirby (1986).

5. Scattering process near impermeable vertical boundaries. In the previous section, it was seen that Poincaré waves normally incident on a channel with vertical side walls are scattered by the sidewalls. This effect arises because the orbital motion in the horizontal plane associated with the Poincaré wave is interrupted by the vertical barrier. In this section, we consider the computationally cleaner case of wave diffraction by a semi-infinite barrier to clarify the nature of the results.

The problem of diffraction of a plane Poincaré wave by a semi-infinite vertical barrier has been discussed by Chambers (1964); we follow his notation here. We consider a barrier lying on the positive x axis and take the incident wave to be of the form

$$\eta_I = \exp\left(ik(x\cos\alpha + y\sin\alpha) + i\omega t\right). \tag{62}$$

The case of incidence parallel to the breakwater corresponds to $\alpha = \pi$. We define the diffraction function as

$$D(r,\theta,\phi) = \frac{1}{\sqrt{\pi}}\exp\left(i\Theta(r,\theta,\phi)\right)\int_{-\infty}^{m(r,\theta,\phi)} \exp\left(-i\gamma^2\right) d\gamma, \tag{63}$$

where $x = r\cos\theta, y = r\sin\theta$, and where

$$\Theta(r,\theta,\phi) = kr\cos(\theta+\phi) - \frac{\pi}{4}, \tag{64}$$

$$m(r,\theta,\phi) = \sqrt{2kr}\cos\tfrac{1}{2}(\theta+\phi). \tag{65}$$

Using this notation, the solution for the total wave field may be written as

$$\eta = D(r,\theta,-\alpha) + k_1 D(r,\theta,\alpha) + k_2 D(r,\theta,-\alpha^*), \tag{66}$$

where α^* is determined by

$$\cos\frac{\alpha^*}{2} = \left(\frac{s-1}{2s}\right)^{1/2}, \qquad \sin\frac{\alpha^*}{2} = -\left(\frac{s+1}{2s}\right)^{1/2}, \tag{67}$$

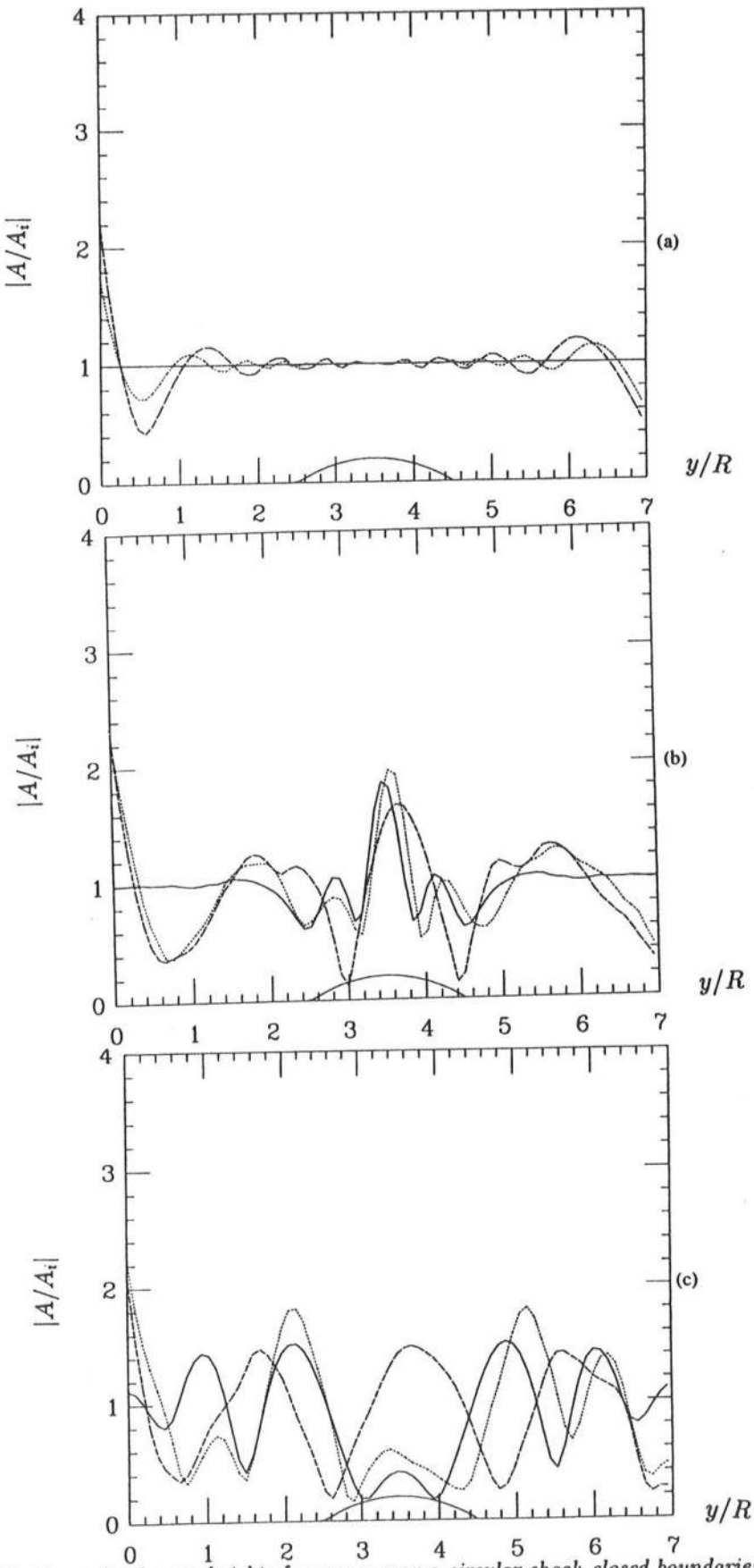

FIG. 9. *Normalized wave heights for waves over a circular shoal; closed boundaries.* (a) $x/R = 1$, (b) $x/R = 3$, (c) $x/R = 5$.

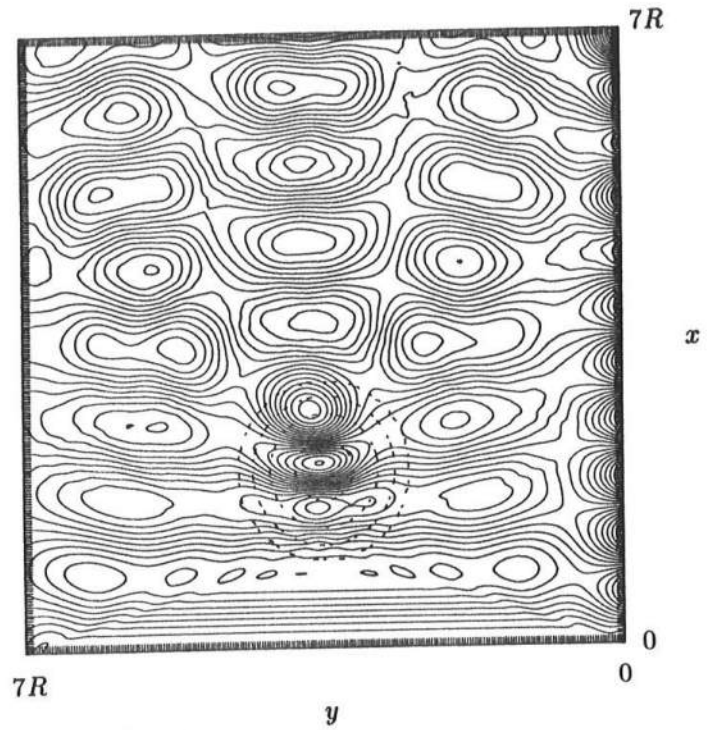

FIG. 10. *Surface elevation contours for wave scattered by a circular shoal; closed boundaries,* $\epsilon = 0.8$.

where $s = (1-\epsilon^2)^{1/2}$. The coefficients of the second and third terms are given by

$$k_1 = \frac{\sin\alpha + i\epsilon\cos\alpha}{\sin\alpha - i\epsilon\cos\alpha}, \tag{68}$$

$$k_2 = \frac{2\sqrt{2}i\sin\frac{\alpha}{2}}{\sin\alpha - i\epsilon\cos\alpha}\left(\frac{1-s}{s}\right)^{1/2}. \tag{69}$$

The first two terms of (66) represent the two components of the Sommerfeld solution that appear in the absence of rotation. The third component has been described by Chambers, but there have not been any plots of the resulting solutions in the literature (at least to these authors' knowledge). The third term represents a motion trapped close to the breakwater and traveling with the breakwater on its right in the northern hemisphere. It thus has the characteristics of the Kelvin wave; in particular, as distance into a shadow region increases, the third term approaches a constant amplitude along the wall, while the first and second terms decay exponentially in amplitude along the wall.

We include a plot of the exact solution for a region $0 \le kx \le 10\pi, -10\pi \le ky \le 10\pi$ and $\alpha = \pi$ in Fig. 11. Since most modern mathematics programs have the ability to compute the error function $\mathrm{erf}(z)$ with z complex, we rewrite D in the form

$$D(r,\theta,\phi) = \frac{(-i)^{1/2}}{2}\exp\left(i\Theta(r,\theta,\phi)\right)\left(1+\mathrm{erf}[(i)^{1/2}m(r,\theta,\phi)]\right). \tag{70}$$

Results are computed and plotted using Mathematica. For contrast, the result of the parabolic model computation for the region $0 \le kx \le 10\pi, -10\pi \le ky \le 10\pi$ is shown in Fig. 12. In the analytic solution, scattering occurs in all directions from the

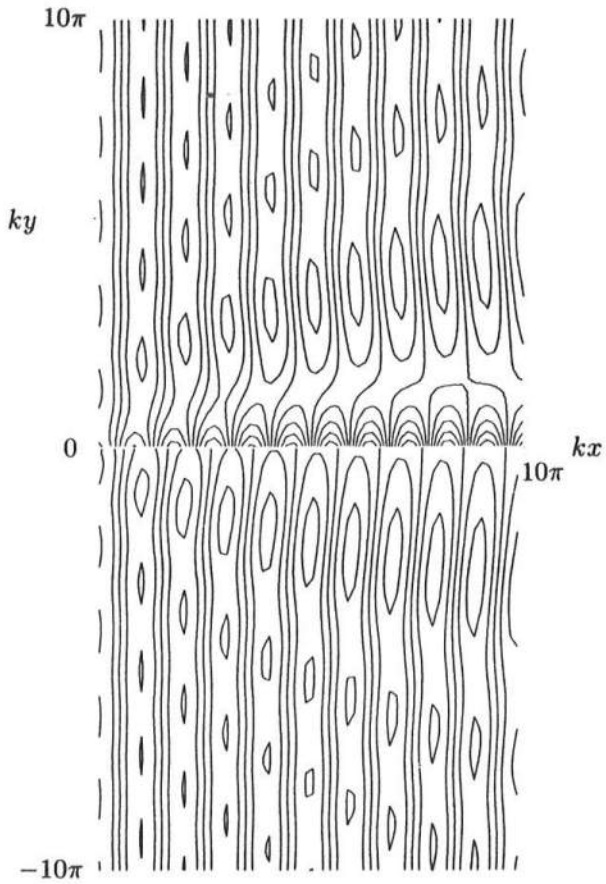

FIG. 11. *Surface elevation contours for scattering by a semi-finite breakwater;* $\epsilon = 0.4$. *Exact solution.*

breakwater tip; however, it is too weak to be of importance in the upwave direction. The parabolic model is not capable of representing this part of the solution. A comparison of Figs. 11 and 12 shows that the diffraction fringes oscillate more rapidly in the transverse direction in the parabolic model computation than in the full solution. The wave form along the breakwater is well predicted by the parabolic model. A comparison of analytic and model wave heights along the breakwater ($x > 0$) is shown in Fig. 13. It is seen that the parabolic model overestimates the height of the Kelvin wave propagating along the upper side of the breakwater, as well as underpredicting the reduced wave height on the lower side.

The more complex pattern of wave height and wave pattern along the $y = 0$ boundary in Fig. 10 occurs because of the interaction of the scattered waves generated over the shoal with the Kelvin wave propagating along the wall. This pattern is highly dependent on the placement of the shoal and the width of the channel relative to the shoal geometry. The height of the shoal relative to the uniform depth region exterior to the shoal also has a strong effect on the distance in x at which waves scattered by the shoal arrive at the side boundaries. Since the number of factors affecting an actual wave pattern along the sidewall is large, we do not pursue a more comprehensive study of the resulting wave patterns here.

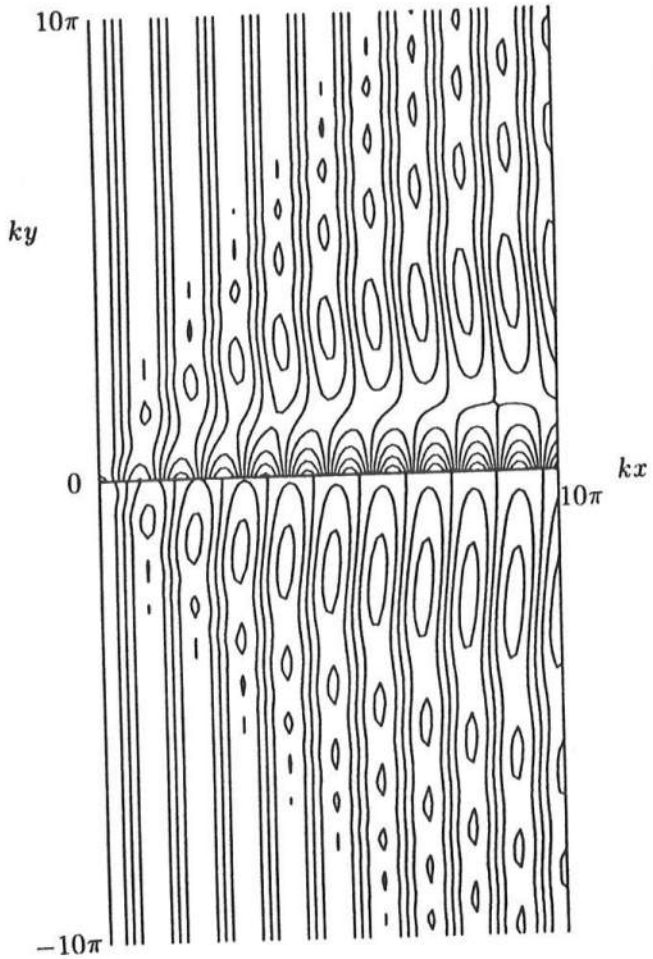

FIG. 12. *Surface elevation contours for scattering by a semi-finite breakwater,* $\epsilon = 0.4$. *Parabolic model computation.*

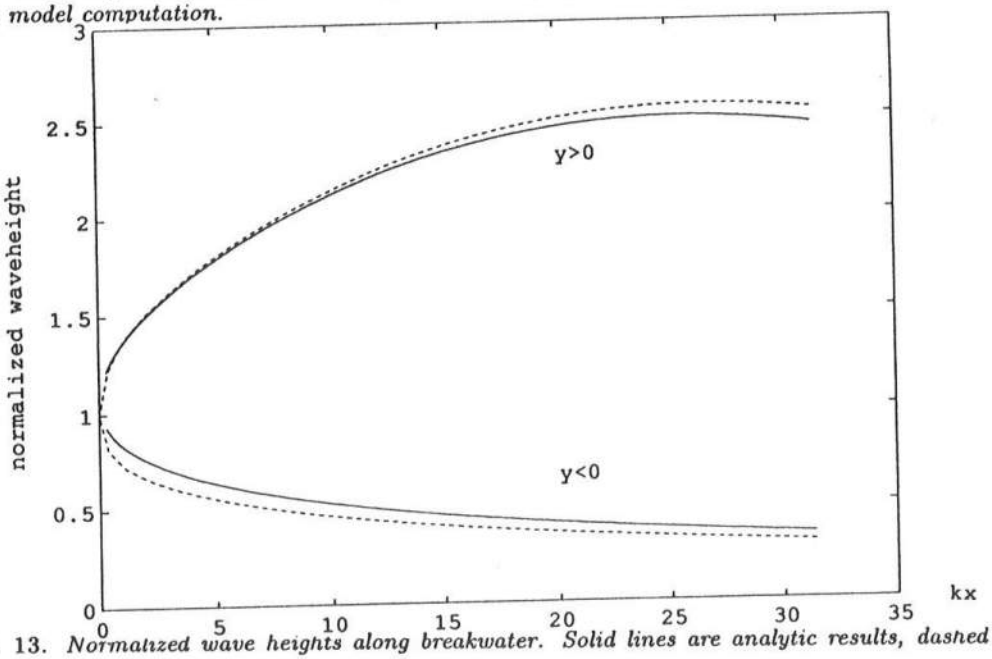

FIG. 13. *Normalized wave heights along breakwater. Solid lines are analytic results, dashed lines are parabolic model computations.*

6. Discussion. While the model developed here is somewhat artificial from an oceanographic point of view, the technique used to derive the model equation from the equation for the fluid pressure is likely to have further application, especially in the area of waves on shear flows, where a velocity potential does not exist (except in special cases) and the stream function representation is available only in two dimensions. Furthermore, the model developed here allows for the development of numerical codes that may be applied to a range of physical phenomena, from short wave refraction-diffraction to tidal motions, with no adjustment of model coefficients required.

The failure of the low-order parabolic approximation to provide accurate prediction of Kelvin and Poincaré modes in a simultaneous calculation indicates that some effort toward obtaining higher-order approximations is warranted, both for the present intermediate depth model and for the usual long wave approximation.

REFERENCES

[1] J. C. W. BERKHOFF (1972), *Computation of combined refraction-diffraction*, in Proc. 13th Internat. Conf. Coastal Engrg., Vancouver, pp. 471–490.

[2] L. G. CHAMBERS (1964), *Long waves on a rotating earth in the presence of a semi-infinite barrier*, Proc. Edinburgh Math. Soc., 14, pp. 25–31.

[3] R. A. DALRYMPLE AND P. A. MARTIN (1992), *Perfect boundary conditions for parabolic water-wave models*, Proc. Roy. Soc. London Ser. A, 437, pp. 41–54.

[4] A. E. GILL (1982), *Atmosphere-Ocean Dynamics*, Academic Press, New York.

[5] J. B. KELLER (1958), *Surface waves on water of non-uniform depth*, J. Fluid Mech., 4, pp. 607–614.

[6] J. T. KIRBY (1986), *Higher-order approximations in the parabolic equation method for water waves*, J. Geophys. Res., 91, pp. 933–952.

[7] ——— (1992), *Discussion of linear surface waves over rotating fluids by T.-K. Tsay*, J. Waterway Port Coastal and Ocean Engrg., 118, pp. 331–333.

[8] J. PEDLOSKY (1979), *Geophysical Fluid Dynamics*, Springer-Verlag, Berlin, New York.

[9] A. C. RADDER (1979), *On the parabolic equation method for water-wave propagation*, J. Fluid Mech., 95, pp. 159–176.

[10] R. SMITH AND T. SPRINKS (1975), *Scattering of surface waves by a conical island*, J. Fluid Mech., 72, pp. 373–384.

[11] T.-K. TSAY (1991), *Linear surface waves over rotating fluids*, J. Waterway Port Coastal and Ocean Engrg., 117, pp. 156–171.